Photoinduced carrier annihilation in silicon pn junction

Toshiyuki Sameshima[1]*, Takayuki Motoki[1], Keisuke Yasuda[1], Tomohiko Nakamura[1],
Masahiko Hasumi[1], and Toshihisa Mizuno[2]

[1]*Tokyo University of Agriculture and Technology, Koganei, Tokyo 184-8588, Japan*
[2]*Kanagawa University, Hiratsuka, Kanagawa 259-1293, Japan*
E-mail: tsamesim@cc.tuat.ac.jp

We report analysis of the photo-induced minority carrier effective lifetime (τ_{eff}) in a p$^+$n junction formed on the top surfaces of a n-type silicon substrate by ion implantation of boron and phosphorus atoms at the top and bottom surfaces followed by activation by microwave heating. Bias voltages were applied to the p$^+$ boron-doped surface with n$^+$ phosphorus-doped surface kept at 0 V. The values of τ_{eff} were lower than 1×10^{-5} s under the reverse-bias condition. On the other hand, τ_{eff} markedly increased to 1.4×10^{-4} s as the forward-bias voltage increased to 0.7 V and then it leveled off when continuous-wave 635 nm light was illuminated at 0.74 mW/cm^2 on the p$^+$ surface. The carrier annihilation velocity S_{p+} at the p$^+$ surface region was numerically estimated from the experimental τ_{eff}. S_{p+} ranged from 4000 to 7200 cm/s under the reverse-bias condition when the carrier annihilation velocity S_{n+} at the n$^+$ surface region was assumed to be a constant value of 100 cm/s. S_{p+} markedly decreased to 265 cm/s as the forward-bias voltage increased to 0.7 V. © 2015 The Japan Society of Applied Physics

1. Introduction

The pn junction is an elementary structure for solar cells, photosensors and transistors.[1–5] The incorporation of impurities at the lattice sites is an essential process technology to form pn junctions. However, it may simultaneously cause photo-induced carrier annihilation defects, which limit the photo-induced carrier lifetime (τ_{eff}). Many passivation technologies have been developed to reduce the density of defects, such as hydrogenation and H$_2$O vapor heat treatment.[6–11] Measurement and analysis methods of τ_{eff} have also been developed to investigate photo-induced carrier annihilation defects such as measurements of the quasi-steady-state photoconductance (QSSPC), microwave photoconductive decay, and microwave absorption of photo-induced carriers caused by continuous light illimunation.[12–19] We have recently reported that τ_{eff} changed with a bias voltage for a metal–oxide–semiconductor (MOS) structure in crystalline silicon.[20] The experimental results suggest that the internal built-in potential distribution can change the probability of photo-induced minority carrier annihilation.

In this paper, we report an investigation of the annihilation properties of photo-induced minority carriers for a pn junction formed in crystalline silicon under the application of bias voltage. We demonstrate a marked change in τ_{eff} from 10^{-6} to 10^{-4} s in the case of light illumination on the surface of the pn junction as a bias voltage is applied from negative (reverse bias) to positive voltages (forward bias). We discuss the field-induced carrier annihilation in the p$^+$ region, and carrier annihilation velocity is numerically estimated.

2. Experimental procedure

Figure 1 shows a schematic of the sample fabrication steps. 17 Ω cm n-type silicon substrates with a thickness of 500 μm and a crystalline orientation of (100) were prepared. The substrates were coated with 100-nm-thick thermally grown SiO$_2$ layers by heating in a wet atmosphere at 1100 °C. The ion implantation of boron atoms was conducted for the top surface of the silicon substrates. The acceleration energy was set at 25 keV to obtain the peak concentration at the interface of the thermally grown SiO$_2$ and silicon. The total dose was 2.0×10^{15} cm^{-2}. Boron atoms at a concentration of $1.0 \times$
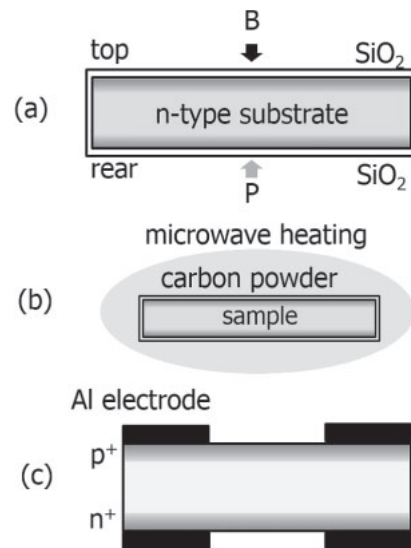
Fig. 1. Schematic sample fabrication steps of (a) boron and phosphorus ion implantations, (b) microwave heating, and (c) SiO$_2$ etching followed by Al electrode formation.

10^{15} cm^{-2} were effectively implanted in the silicon substrates. The ion implantation of phosphorus atoms at 75 keV was also conducted for the rear surface of the silicon substrates. Phosphorus atoms at a concentration of 1.0×10^{15} cm^{-2} were effectively implanted in the silicon substrates. Most of boron and phosphorus atoms were located within 60 nm from the silicon surfaces. The implanted samples with the SiO$_2$ layers coated on the surfaces were subsequently heated by microwave irradiation using a commercial 2.45 GHz microwave oven at 1000 W for a duration of 150 s.[21] The samples were completely covered with carbon powders 2-μm-diameter for effective heating and placed on a quartz glass substrate with low heat conductivity to keep the heat energy in the sample region. The SiO$_2$ layers prevented the incorporation of other materials such as carbon into silicon.[22] The SiO$_2$ layers were then removed by dipping the samples in 5% dilute hydrofluoric acid. Al electrodes were subsequently formed at the top and rear surfaces to enable the application bias voltages to the samples. The Al electrodes had a loop shape with an open
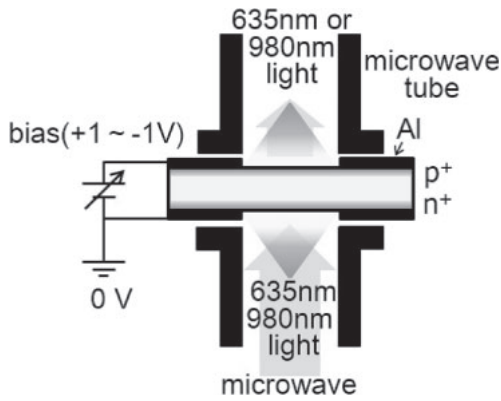
Fig. 2. Schematic 9.35-GHz-microwave-transmittance measurement system.

middle region of $1.0 \times 2.3 \, cm^2$ for microwave transmission measurements.

Optical reflectivity spectra were measured between 250 and 1000 nm using a conventional spectrometer to investigate the crystalline volume ratio X_c in the ion-implanted surface regions. The SiO_2 layers were removed for precise measurement. The spectra were analyzed using a numerical calculation program, which was constructed on the basis of the optical interference effect for an air/multiple Si layers/Si substrate structure.[23,24] The optical reflectivity on the silicon surface depends on the complex refractive index of each silicon layer. Using the effective dielectric model, the complex refractive index with the crystalline volume ratio X_c is determined by combining the crystalline refractive index $\tilde{n}_c$ with the amorphous refractive index $\tilde{n}_a$ as[25,26]

$$\tilde{n}_f = X_c \tilde{n}_c + (1 - X_c) \tilde{n}_a. \tag{1}$$

The thickness and crystalline volume ratio were changed for each layer to calculate the reflectivity. The most probable in-depth distribution of the crystalline volume ratio was obtained by fitting the calculated reflectivity spectra to the experimental reflectivity spectra.

To investigate the carrier lifetime and carrier annihilation probability, we used a 9.35-GHz-microwave-transmittance measurement system, as shown schematically in Fig. 2.[17,18,20,27] The system had waveguide tubes, which had a narrow gap where a sample was placed. Continuous-wave (CW) 635 and 980 nm laser diode (LD) lights were introduced into the waveguide tubes. The light intensities were set at 0.74 and 0.48 mW/cm^2 on the sample surface for 635 and 980 nm lights, respectively, to realize the same photon flux between the two different wavelengths. The microwave transmittances in a dark field T_d were detected to obtain the majority carrier density N_M. In our previous reports,[17,18] a finite-element numerical calculation program with a Fresnel-type microwave interference effect between silicon surfaces and the free carrier absorption was used to estimate N_M, which is obtained by fitting the calculated T_d to the experimental T_d. The microwave transmittance under the light illumination of the boron-implanted surface $T_p(p^+)$ was also measured to obtain the photo-induced minority carrier effective lifetime $\tau_{eff}(p^+)$ in the cases of light illumination of the boron-implanted p^+ surface. $\tau_{eff}(p^+)$ was precisely obtained by the numerical analysis of T_d and $T_p(p^+)$, while it is approximately proportional to $\ln T_d/T_p(p^+)$.[19] The photo-

induced minority carrier effective lifetime in the case of light illumination of the phosphorus-implanted n^+ surface $\tau_{eff}(n^+)$ was also obtained from T_d and the microwave transmittance under the light illumination of the n^+ surface $T_p(n^+)$. The measurement system had a high dynamic τ_{eff} range in the time range from 10^{-6} to 10^{-2} s. The penetration depth was about 2.7 and 120 µm for 635 and 980 nm lights, respectively.[25] The photo-induced minority carrier density n_m is governed by the carrier generation ratio G and τ_{eff},

$$n_m = \tau_{eff} G. \tag{2}$$

G generally depends on the light intensity and optical reflectance at the sample surface. In advance of the present experiment, the G value was determined using two control samples with high τ_{eff} values of 1×10^{-3}–2×10^{-3} s with surfaces coated with 100-nm-thick thermally grown SiO_2 layers and with 1-nm-thick SiO_2 layers formed by liquid water heat treatment, whose optical reflectivity spectrum was almost the same as that of bare silicon.[28] The multiply periodic pulsed illumination method directly gave τ_{eff} values of the two control samples under the detection limit of the measurement of τ_{eff} of 2×10^{-5} s.[19] Using the τ_{eff} values of the control samples, the G values were determined for samples with surfaces coated with SiO_2 and bare surfaces in the present CW light illumination measurement system. The best coincident between experimental T_d/T_p and calculated T_d/T_p results in the most probable τ_{eff} for each illumination mode. The microwave-transmittance measurements with CW light illumination were carried out for initial, ion-implanted, microwave-heated samples. The SiO_2 layer still remained in the measurements. The microwave-transmittance measurements with CW light illumination were also carried out in the case of open and short circuits between the Al electrodes formed on the p^+ and n^+ surfaces of the samples with bare surfaces. Moreover, they were carried out with different bias voltages applied to the Al electrode formed on the p^+ surface while the Al electrode formed on the n^+ surface at 0 V. The electrical current was also measured as a function of bias voltage.

3. Results and discussion

Figure 3 shows experimental optical reflectivity spectra of the (a) initial, as-boron-, and phosphorus-ion-implanted surfaces and (b) microwave heated boron- and phosphorus-ion implanted surfaces. The SiO_2 layers were removed for all samples for precise measurements. Two large peaks of E_1 and E_2 caused by the large joint density of states at the X point in the Brillouin zone of crystalline silicon appeared at 340 and 275 nm for the initial sample. On the other hand, the peak heights of E_1 and E_2 became small upon boron ion implantation. Decreases in the heights of the peaks indicate the partial amorphization of the surface region for the boron-implanted surface. Moreover, no E_1 and E_2 peaks were observed in the case of phosphorus implantation, as shown in Fig. 3(a). Phosphorus implantation caused complete amorphization of the surface region. On the other hand, the microwave heating changed the optical reflectivity spectra of the ion-implanted samples similar to the optical reflectivity spectrum of the initial sample having the E_1 and E_2 peaks, as shown in Fig. 3(b). The amorphized surface regions were recrystallized by the microwave heating. Analysis of the reflectivity spectra indicated that the boron ion implantation
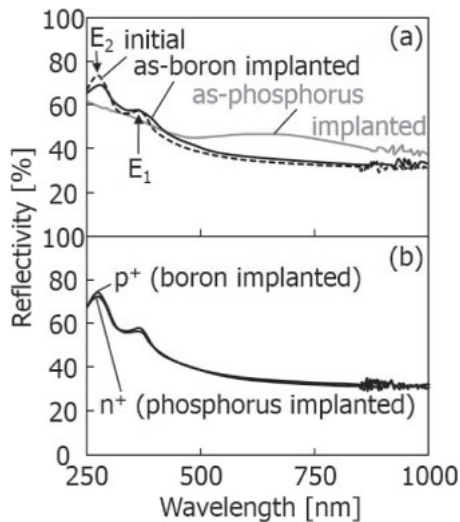
Fig. 3. Experimental optical reflectivity spectra of (a) initial, as-boron- and phosphorus-ion implanted surfaces and (b) microwave heated boron- and phosphorus-ion implanted surfaces.

Fig. 4. $\tau_{eff}(p^+)$ (open circles) and $\tau_{eff}(n^+)$ (solid circles) measured by light illumination at (a) 635 and (b) 980 nm for each process step of initial, as-ion implanted, microwave annealed, open and short circuit conditions between the Al electrodes.

decreased X_c to 0.3 in the top 5 nm region and 0.95 from a depth of 5 to 40 nm because of boron implantation with a high peak concentration of 3×10^{20} cm^{-3}. The phosphorus ion implantation decreased X_c to 0.0 in the top 35 nm region and 0.7 from a depth of 35 to 50 nm. On the other hand, the microwave heating at 1000 W for 150 s increased X_c to 1.0 in the boron- and phosphorus-implanted surface regions. The microwave heating effectively recrystallized the silicon surface regions.

The initial sample had a microwave transmissivity in a dark field T_d of 26.1% because of the high resistivity of 17 Ω cm of the silicon substrate. N_M and the Fermi level were estimated to be 2.8×10^{14} cm^{-3} and 0.826 eV, respectively, from the valence band edge. T_d was not changed by boron and phosphorus implantation because carriers were not generated in the as-implanted state. On the other hand, T_d was markedly decreased to 6.8% by the microwave heating. Carriers generated by the activation of boron- and phosphorus-doped surface regions caused substantial absorption of the incident microwaves. The analysis of T_d indicated that the sheet resistivity decreased from 340 (initial) to 88 Ω/sq. Doped surface regions with low resistivities were successfully formed by the microwave heating.

Figure 4 shows $\tau_{eff}(p^+)$ (open circles) and $\tau_{eff}(n^+)$ (solid circles) measured by light illumination at (a) 635 and (b) 980 nm after each process step for the initial, as-ion im- planted, microwave-annealed, open-, and short-circuit con- ditions between the Al electrodes. τ_{eff} was high at 1.5×10^{-3} s in the cases of 635 and 980 nm light illumination of the p$^+$ and n$^+$ surfaces for the initial sample. The silicon surfaces were well passivated by the thermally grown SiO$_2$ layers. Boron and phosphorus ion implantation decreased $\tau_{eff}(p^+)$ and $\tau_{eff}(n^+)$ to 1.1×10^{-6} and 1.0×10^{-6} s, respectively, in the case of 635 nm light illumination. $\tau_{eff}(p^+)$ and $\tau_{eff}(n^+)$ were also decreased to 7.5×10^{-6} and 5.0×10^{-6} s, respec- tively, in the case of 980 nm light illumination. Boron and phosphorus ion implantation caused serious damage to the silicon surface regions which increased the carrier annihila- tion probability on the surfaces. On the other hand, $\tau_{eff}(p^+)$
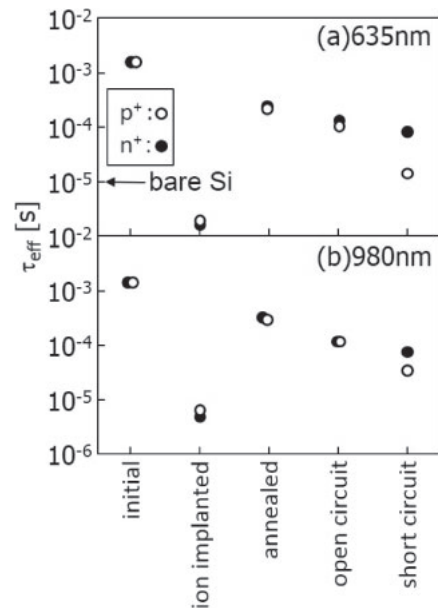
and $\tau_{eff}(n^+)$ were markedly increased by the microwave heating. They were 2.5×10^{-4} and 2.6×10^{-4} s in the case of 635 nm light illumination and 2.9×10^{-4} and 3.2×10^{-4} s in the case of 980 nm light illumination, respectively. Through recrystallization and activation of the ion implanted surface regions by microwave heating, the density of carrier annihilation defects was decreased. Under the open circuit condition of the Al electrodes formed at the surface after removing the thermally grown SiO$_2$ layers, $\tau_{eff}(p^+)$ under the 635 nm illumination was 1.1×10^{-4} s, which was lower than the values of $\tau_{eff}(p^+)$ as-microwave-heated conditions. $\tau_{eff}(n^+)$ under the 635 nm illumination was 1.3×10^{-4} s, which was slightly larger than the values of $\tau_{eff}(p^+)$. $\tau_{eff}(p^+)$ under the 980 nm illumination was 1.2×10^{-4} s and $\tau_{eff}(n^+)$ under the 980 nm illumination was 1.1×10^{-4} s. $\tau_{eff}(p^+)$ and $\tau_{eff}(n^+)$ under the open circuit condition were lower than those for the as-microwave-heated sample with thermally grown SiO$_2$ layers, while they were higher than that of about 1.0×10^{-5} s for n-type silicon substrates with bare surfaces. An interesting phenomenon was observed under the short circuit condition of the Al electrodes. The $\tau_{eff}(p^+)$ under the 635 nm light illumination markedly decreased to 1.2×10^{-5} s. This indicates that the density of minority carrier was very low when 635 nm light was illuminated on the p$^+$ surface. On the other hand, $\tau_{eff}(n^+)$ under the 635 nm illumination was 8.3×10^{-5} s, which was comparable to $\tau_{eff}(n^+)$ under the open circuit condition. In a similar manner, $\tau_{eff}(p^+)$ and $\tau_{eff}(n^+)$ under the 980 nm illumination were 3.5×10^{-5} and 8.0×10^{-5} s, respectively. These results in Fig. 4 show that the short circuit electrical condition decreased $\tau_{eff}(p^+)$.

Figure 5 shows $\tau_{eff}(p^+)$ and $\tau_{eff}(n^+)$ in the cases of light illumination at 635 nm (open circles) and 980 nm (solid circles) as a function of the bias voltage applied to the Al electrodes formed at the p$^+$ regions while keeping the Al electrodes formed in the n$^+$ regions at 0 V. $\tau_{eff}(p^+)$ was lower than 1×10^{-5} s for the bias voltage of lower than
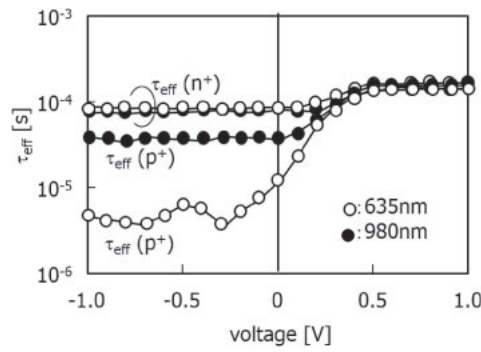
Fig. 5. $\tau_{\text{eff}}(\text{p}^+)$ and $\tau_{\text{eff}}(\text{n}^+)$ in the cases of light illumination at 635 (open circles) and 980 nm (solid circles) as a function of the bias voltage applied to the Al electrodes formed at the p^+ regions with keeping the Al electrodes formed at the n^+ regions at 0 V.

Fig. 6. (a) Electrical current as a function of applied voltage (I–V) in the conditions of the dark field, 635 and 980 nm light illumination of the p^+ surfaces and (b) magnifications of I–V characteristics for the negative current region.

0 V (reverse-bias condition) in the case of 635 nm light illumination. It markedly increased to 1.4×10^{-4} s as the bias voltage increased from 0 to 0.7 V (forward-bias condition) and leveled off above 0.7 V. On the other hand, $\tau_{\text{eff}}(\text{p}^+)$ ranged from 3.1×10^{-5} to 3.9×10^{-5} s lower than 0 V or 0 V in the case of the 980 nm light illumination. These values were higher than those in the case of 635 nm light illumination. $\tau_{\text{eff}}(\text{p}^+)$ in the case of 980 nm light illumination increased to 1.5×10^{-4} s as the bias voltage increased from 0 to 0.7 V and leveled off above 0.7 V. When 635 nm light was illuminated on the n^+ surfaces, $\tau_{\text{eff}}(\text{n}^+)$ ranged from 8.1×10^{-5} to 8.4×10^{-5} s for a bias voltage lower than 0 V or 0 V, in contrast to the low $\tau_{\text{eff}}(\text{p}^+)$ in the case of 635 nm light illumination. $\tau_{\text{eff}}(\text{n}^+)$ increased to 1.6×10^{-4} s as the bias voltage increased from 0 to 0.7 V and leveled off above 0.7 V. $\tau_{\text{eff}}(\text{n}^+)$ in the case of 980 nm light illumination had a similar behavior to $\tau_{\text{eff}}(\text{n}^+)$ in the case of 635 nm light illumination. $\tau_{\text{eff}}(\text{n}^+)$ ranged from 7.4×10^{-5} to 7.7×10^{-5} s for a bias voltage of lower than 0 V or at 0 V. It increased to 1.5×10^{-4} s as the bias voltage increased from 0 to 0.7 V and leveled off above 0.7 V. The results in Fig. 5 suggest that τ_{eff} was sensitive to the electrical-field effect caused by the applied voltage. $\tau_{\text{eff}}(\text{p}^+)$ had a small value of lower than 1×10^{-5} s only in the case of 635 nm light illumination under the reverse-bias condition. On the other hand, the application of a sufficiently high forward-bias voltage resulted in τ_{eff} having similar values ranging from 1.4×10^{-4} to 1.6×10^{-4} s among four light illumination modes.

Figure 6 shows (a) the electrical current as a function of applied voltage (I–V) under the conditions of a dark field and 635 and 980 nm light illumination of the p^+ surfaces and (b) a magnification of the I–V characteristics in the negative current region. Rectified diode characteristics are observed for every case. The results in Fig. 6 therefore show that an internal potential barrier was formed by the p^+-doped region in the n-type substrates. Similar photo-induced negative current characteristics were observed for bias ranging from -1 to 0.35 V under 635 and 980 nm light illumination with short circuit currents I_{sc} of -3.14×10^{-3} and -3.13×10^{-3} A, respectively. A photo-induced current and the photovoltaic effect were observed. Similar I–V characteristics were obtained in the cases of the 635 and 980 nm light illumination of the n^+ surface, while I_{sc} was slightly low of -2.3×10^{-3} and -2.4×10^{-3} A.
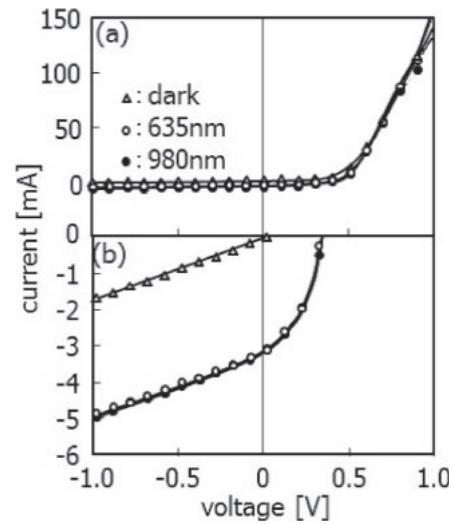
The results in Figs. 4 and 5 clearly show that τ_{eff} strongly depended on the bias voltage. Low values of τ_{eff} were observed for every illumination mode under the conditions of reverse or zero bias voltage, which are associated with the high built-in potential barrier formed under the p^+-doped region. In particular, the values of $\tau_{\text{eff}}(\text{p}^+)$ in the case of the 635 nm light illumination case were very low, 1.2×10^{-5} s or lower, as shown in Fig. 5. On the other hand, application of the forward-bias voltage increased τ_{eff}. $\tau_{\text{eff}}(\text{p}^+)$ in the case of 635 nm light illumination case markedly increased to 1.4×10^{-4} s, as shown in Fig. 5. τ_{eff} had similar values ranging from 1.4×10^{-5} to 1.6×10^{-6} s among the four illumination modes above a forward-bias of 0.7 V. A built-in potential estimated to be 0.83 eV was formed in the p^+n junction region at a bias of 0 V in this samples. There were a positively charged region in the depletion region and negatively charged-up region in the p^+ region adjacent to the interface of the p^+n junction. According to the classical theory,[29–31] the quasi-Fermi potential of the photo-induced hole minority carriers was almost constant and only changed by at most 0.006 eV over the depletion region because the photo-induced current density was low, 1.4×10^{-3} A cm^{-2}, at a bias of 0 V, under the present experimental conditions, the carrier generation ratio for 635 nm illumination was 2.45×10^{15} cm^{-2} s^{-1}. The τ_{eff} of 1.2×10^{-5} s at 0 V gives an average photo-induced hole carrier volume density of 5.9×10^{11} cm^{-3}. When all of the photo-induced hole carriers contributed to the photo-induced current, the hole carrier velocity was given as 1.5×10^4 cm/s by the current density, hole carrier density, and elemental charge. The potential change was estimated as at most 0.006 eV from the hole carrier velocity, the hole mobility of 450 cm^2 V^{-1} s^{-1}, and the depletion width of 2.0×10^{-4} cm, which was obtained from N_{M} of 2.8×10^{14} cm^{-3}. Therefore the diffusion of photo-induced hole minority carriers can be considered to satisfy the flat band condition in the depletion region. We previously developed a finite-element numerical calculation program that included the theories of carrier generation associated with the optical absorption coefficients as well as carrier

diffusion between the two p$^+$/n and n/n$^+$ interfaces, where the annihilation velocities S_{p^+} and S_{n^+} were set at the p$^+$/n and n/n$^+$ interfaces.[32] The density of photo-induced minority carriers as a function of the depth x from the p$^+$/n interface in the steady state under the illumination of the p$^+$ region with CW light is given as

$$D \frac{\partial^2 n_m(x)}{\partial x^2} + \frac{n_m(x)}{\tau_b} - g(x) = 0, \qquad (3)$$

where τ_b, $n_m(x)$, $g(x)$, and D are the bulk lifetime, the carrier volume density, the carrier generation rate at a depth of x, and the diffusion constant, respectively. Carrier generation occurs in the substrate bulk and which depends on the optical absorption coefficient at a certain light wavelength. $g(x)$ is given with the optical penetration depth d of light as

$$g(x) = \frac{G}{d} e^{-x/d}. \qquad (4)$$

The boundary conditions are given as

$$D \left. \frac{\partial n_m(x)}{\partial x} \right|_{x=0} = S_{p^+}(V) n_m(0) - g(0)\Delta x, \qquad (5a)$$

$$D \left. \frac{\partial n_m(x)}{\partial x} \right|_{x=L} = -S_{n^+} n_m(L) - g(L)\Delta x. \qquad (5b)$$

where L is the thickness of the semiconductor substrate between the p$^+$/n and n/n$^+$ interfaces of and Δx is the unit lattice length for 2×10^{-5} cm in the present calculation. n_m was obtained by the integration of $n_m(x)$ from 0 to L. τ_{eff} was obtained by dividing the calculated n_m by G. We assumed that an ohmic junction was formed at the n/n$^+$ interface and S_{n^+} was constant for every bias voltage. The most probable $S_{p^+}(V)$ and S_{n^+} as a function of bias voltage were analyzed by fitting calculated τ_{eff} to experimental τ_{eff} measured with four illumination modes. In the present cases, we assumed that τ_b was long enough, and that carrier annihilation was governed only by the annihilation velocity at the surfaces.

Figure 7 shows $S_{p^+}(V)$ as a function of bias voltage. S_{n^+} is also presented by a solid line. $S_{p^+}(V)$ was high, ranging from 4000 to 7200 cm/s, under the conditions of reverse and zero bias voltage. It decreased to 265 cm/s, which was comparable to the value of S_{n^+} of 100 cm/s, as the bias voltage increased to 0.7 V. In general, the excess carrier annihilation rate is determined by the active carrier recombination defect density per unit area, the carrier capture crosssection, the carrier velocity and the excess electron and hole carrier densities.[29,33–35] In the present work, high values of $S_{p^+}(V)$ appeared under the application of the reverse and zero bias voltage, high built-in potential associated with the negative charging in the p$^+$ region and positive charging in the depletion region of the n-type substrate. Although details of the physics are not clear yet, we suggest that negative charging in the p$^+$ region increases $S_{p^+}(V)$ to a high value. There are many defect states in the band gap in the p$^+$ region because of the heavy doping. Under the neutral condition, the Fermi level locates close to the valence band edge. Most of the defect states are occupied and not active for carrier recombination. The negative charging associated with a high density of acceptor charges of $\sim 10^{20}$ cm^{-3} increases the Fermi level to the deep level and is expected to increase the density of unoccupied and active defect states for carrier recombination.[29] Under the reverse-bias or zero-bias con-
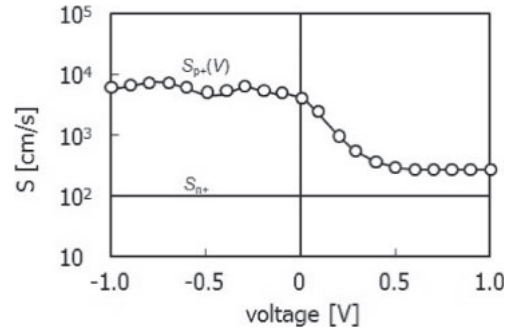
Fig. 7. Carrier annihilation velocity at the p$^+$ interface $S_{p^+}(V)$ as a function of bias voltage. The carrier annihilation velocity at the n$^+$ interface S_{n^+} is also presented by a solid line.

dition, the injected excess hole and electron carriers should be effectively recombined in the negatively charged region owing to the high density of active defects. The high $S_{p^+}(V)$ effectively decreased n_m in the n-type substrate, especially in the case of 635 nm light illumination because photo-induced carriers were generated near the p$^+$/n interface because of the low value of d of 2.7 μm. The $\tau_{eff}(p^+)$ consequently has low values of less than 1×10^{-5} s, as shown in Fig. 5. On the other hand, 980 nm light illumination resulted in photo-induced carriers in the region with d of 120 μm. n_m maintained high values because of the time required for diffusion from the deep carrier generation region to the p$^+$ interface. Therefore $\tau_{eff}(p^+)$ had high values ranging from 3.4×10^{-5} to 3.9×10^{-5} s in the case of 980 nm light illumination, as shown in Fig. 5. Moreover, photo-induced carriers generated by light illumination of the n$^+$ region traversed across the silicon substrate to reach the p$^+$ interface. The long diffusion distance allowed high values of $\tau_{eff}(n^+)$.

The application of forward-bias voltage reduces the negative charging in the p$^+$ region facing the pn junction. The Fermi level decreases to the valence edge, and defect states are expected to become occupied and inactive for carrier recombination. We believe that the reduction of negative charging in the p$^+$ region is the reason why the application of the forward-bias voltage decreased $S_{p^+}(V)$, as shown in Fig. 7. $S_{p^+}(V)$ is minimum when the negative charge density is negligible small. The lowest value of $S_{p^+}(V)$ of 265 cm/s at 0.7 V suggests that the flat band condition is established. Similar values of the lowest $S_{p^+}(V)$ of 265 cm/s, and S_{n^+} of 100 cm/s resulted in similar τ_{eff} among the four illumination modes, as shown in Fig. 5. Under the assumption of the flat band condition, the S value was estimated to be 16 cm/s for the initial samples coated with thermally grown SiO$_2$ layers. Thermally grown SiO$_2$ effectively passivated the silicon surfaces. The lowest $S_{p^+}(V)$ and S_{n^+} were larger than the S values of the initial samples. A substantial density of defect states remained in the p$^+$- and n$^+$-doped regions. On the other hand, they were much lower than S of 50000 cm/s at the as-boron-implanted surface and 70000 cm/s at the as-phosphorus-implanted surface for the as-ion-implanted samples so that the values of τ_{eff} were very low, on the order of 10^{-6} s, as shown in Fig. 4. The activation process by microwave heating markedly reduced the density of carrier annihilation defect states.

The present investigation reported the in τ_{eff} with the bias voltage in a p$^+$n junction formed on the top surfaces of n-type

silicon substrates. The model of the electrical field-induced enhancement of carrier annihilation velocity in the p$^+$ region was proposed. It was found by analysis that $S_{p^+}(V)$ ranged from 4000 to 7200 cm/s under the reverse-bias condition between 0 and -1 V. A decrease in $S_{p^+}(V)$ to 265 cm/s under the forward-bias condition above 0.7 V was also found by analysis. The results suggest the present measurement system is useful to investigate the photoinduced carrier annihilation properties of semiconductors in which the built-in potential is distributed.

4. Conclusions

We reported an investigation of the annihilation properties of photo-induced minority carriers for a pn junction formed in 500-μm-thick, 17 Ω cm, n-type crystalline silicon with a crystalline orientation of (100) under the application of bias voltage. The p$^+$n junction was formed in the top surface region of the silicon substrates coated with 100-nm-thick thermally grown SiO$_2$ layers by boron and phosphorus ion implantation with a dose of 1×10^{15} cm^{-2} followed by microwave heating using a commercial 2.45 GHz microwave oven at 1000 W for a duration of 150 s. The ion-implanted surface regions were recrystallized, and boron and phosphorus atoms were effectively activated with a sheet resistivity of 88 Ω/sq. τ_{eff} was markedly decreased from 1.5×10^{-3} to about 1.0×10^{-6} s in the case of 635 nm light illumination of p$^+$ and n$^+$ surfaces subjected by ion implantation, while it was increased to about 2.5×10^{-4} s by microwave heating. The density of carrier annihilation defects was decreased by microwave annealing. Rectified characteristics, a photo induced current and the photo-voltaic effect were observed in the I–V characteristics under the application of reverse and forward-bias voltages to the Al electrodes with a loop shape formed at the p$^+$ and n$^+$ surfaces after removing the SiO$_2$ layers. Changes in $\tau_{eff}(p^+)$ and $\tau_{eff}(n^+)$ were observed upon the application of reverse and forward-bias voltages. $\tau_{eff}(p^+)$ in the case of 635 nm light illumination was lower than 1×10^{-5} s for the reverse-bias condition, while it markedly increased to 1.4×10^{-4} s as the forward-bias voltage increased from 0 to 0.7 V and the leveled off. On the other hand, $\tau_{eff}(p^+)$ ranged from 3.1×10^{-5} to 3.9×10^{-5} s for the reverse-bias condition in the case of the 980 nm light illumination. It increased to 1.5×10^{-4} s as the forward-bias voltage increased from 0 to 0.7 V and leveled off. $\tau_{eff}(n^+)$ ranged from 8.1×10^{-5} to 8.4×10^{-5} s for the reverse bias condition in the cases of 635 nm light illumination, while it increased to 1.6×10^{-4} s as the forward-bias voltage increased from 0 to 0.7 V and then leveled off. $\tau_{eff}(n^+)$ ranged from 7.4×10^{-5} to 7.7×10^{-5} s for the reverse-bias condition in the case of 980 nm light illumination, while it increased to 1.6×10^{-4} s as the forward-bias voltage increased from 0 to 0.7 V and then leveled off. The numerical analysis of $\tau_{eff}(p^+)$ and $\tau_{eff}(n^+)$ gave a high values of $S_{p^+}(V)$ from 4000 to 7200 cm/s under the conditions of reverse and zero bias voltage, while it decreased to 265 cm/s, when the forward-bias voltage increased from 0 to 0.7 V and then leveled off under the assumption of a constant value of S_{n^+} of 100 cm/s. The high values of $S_{p^+}(V)$ for the reverse-bias condition were interpreted to be due to an increase in the density of unoccupied and active defect states caused by electrical negative charging in the p$^+$ region. $S_{p^+}(V)$ decreased to

265 cm/s, which was probably limited by the intrinsic density of defect states, when a forward-bias voltage of 0.7 V was applied probably because a flat-band condition was established at the p$^+$/n interface. The present measurement system will be useful for investigating the photo-induced carrier annihilation properties of semiconductor in which the built-in potential is distributed.

1) S. M. Sze, *Semiconductor Devices* (Wiley, New York, 1985) Chap. 3.
2) M. A. Green, Prog. Photovoltaics **17**, 183 (2009).
3) E. A. G. Webster, L. A. Grant, and R. K. Henderson, IEEE Trans. Electron Devices **60**, 1188 (2013).
4) M. Mehrotra, J. C. Hu, A. Jain, W. Shiau, V. Reddy, S. Aur, and M. Rodder, IEDM Tech. Dig., 1999, p. 419.
5) K. Goto, T. Yamamoto, T. Kubo, M. Kase, Y. Wang, T. Lin, S. Talwar, and T. Sugii, IEDM Tech. Dig., 1999, p. 931.
6) I.-W. Wu, A. G. Lewis, T.-Y. Huang, and A. Chiang, IEEE Electron Device Lett. **10**, 123 (1989).
7) B. L. Sopori, Sol. Energy Mater. Sol. Cells **41–42**, 159 (1996).
8) D. Jousse, S. L. Delage, and S. S. Iyer, Philos. Mag. B **63**, 443 (1991).
9) T. Sameshima and M. Satoh, Jpn. J. Appl. Phys. **36**, L687 (1997).
10) T. Sameshima, M. Satoh, K. Sakamoto, K. Ozaki, and K. Saitoh, Jpn. J. Appl. Phys. **37**, 4254 (1998).
11) K. Sakamoto and T. Sameshima, Jpn. J. Appl. Phys. **39**, 2492 (2000).
12) G. S. Kousik, Z. G. Ling, and P. K. Ajmera, J. Appl. Phys. **72**, 141 (1992).
13) J. M. Borrego, R. J. Gutmann, N. Jensen, and O. Paz, Solid-State Electron. **30**, 195 (1987).
14) H. Daio and F. Shimura, Jpn. J. Appl. Phys. **32**, L1792 (1993).
15) M. Boulou and D. Bois, J. Appl. Phys. **48**, 4713 (1977).
16) Y. Ogita, J. Appl. Phys. **79**, 6954 (1996).
17) T. Sameshima, H. Hayasaka, and T. Haba, Jpn. J. Appl. Phys. **48**, 021204 (2009).
18) T. Sameshima, R. Ebina, K. Betsuin, Y. Takiguchi, and M. Hasumi, Jpn. J. Appl. Phys. **52**, 011801 (2013).
19) T. Sameshima, T. Nagao, S. Yoshidomi, K. Kogure, and M. Hasumi, Jpn. J. Appl. Phys. **50**, 03CA02 (2011).
20) T. Sameshima, J. Furukawa, T. Nakamura, S. Shigeno, T. Node, S. Yoshudomi, and M. Hasumi, Jpn. J. Appl. Phys. **53**, 031301 (2014).
21) M. Hasumi, T. Nakamura, S. Yoshidomi, and T. Sameshima, Jpn. J. Appl. Phys. **53**, 05FV05 (2014).
22) T. Sameshima, M. Maki, M. Takiuchi, N. Andoh, N. Sano, Y. Matsuda, and Y. Andoh, Jpn. J. Appl. Phys. **46**, 6474 (2007).
23) M. Born and E. Wolf, *Principles of Optics* (Pergamon, New York, 1974) Chaps. 1 and 13.
24) T. Sameshima, Y. Matsuda, Y. Andoh, and N. Sano, Jpn. J. Appl. Phys. **47**, 1871 (2008).
25) E. D. Palk, *Handbook of Optical Constants of Solids* (Academic Press, London, 1985) pp. 562 and 577.
26) J. R. Chelikowsky and M. L. Cohen, Phys. Rev. B **10**, 5095 (1974).
27) T. Sameshima, J. Furukawa, and S. Yoshidomi, Jpn. J. Appl. Phys. **52**, 041303 (2013).
28) T. Nakamura, M. Hasumi, and T. Sameshima, submitted to Jpn. J. Appl. Phys.
29) A. S. Groove, *Physics and Technology of Semiconductor Devices* (Wiley, New York, 1967) Chap. 5.
30) Y. Taur and T. Ning, *Fundamental of Modern VLSI Physics* (Cambridge University Press, Cambridge, U.K., 1998) Chap. 2.
31) K. R. McIntosh, IEEE Trans. Electron Devices **54**, 346 (2007).
32) T. Sameshima and S. Shibata, Jpn. J. Appl. Phys. **53**, 061301 (2014).
33) J. G. Simmons and G. W. Taylor, J. Phys. C **7**, 3051 (1974).
34) M. Gunes, Y. M. Li, R. M. A. Dawson, C. M. Fortmann, and C. R. Wronski, Proc. 23rd IEEE Photovoltaic Specialists Conf., 1993, p. 885.
35) H. A. Mar and J. G. Simmons, Phys. Rev. B **11**, 775 (1975).